PAPER

How protonation and deprotonation of 9-methylguanine alter its singlet O₂ addition path: about the initial stage of guanine nucleoside oxidation†

Wenchao Lu,[ab] Huayu Teng[a] and Jianbo Liu*[ab]

Mutagenicity of singlet O_2 is due to its oxidatively generated damage to the guanine nucleobases of DNA. Oxidation of neutral guanosine has been assumed to be initiated by the formation of a transient 4,8-endoperoxide *via* a Diels−Alder cycloaddition of singlet O_2. Protonation and deprotonation of guanosine represent another factor related to DNA damage and repair. Herein, 9-methylguanine was utilized as a model substrate to mimic the correlation between singlet O_2 oxidation of the nucleoside and its ionization states, both in the absence and in the presence of water ligands. We used guided-ion-beam scattering tandem mass spectrometry to detect and quantify transient intermediates at room temperature. To provide a reliable description of reaction potential surfaces, different levels of theory including restricted and unrestricted density functional theory, CCSD(T), MP2, and multi-reference CASSCF and CASMP2 were applied. By means of molecular potential, kinetic and direct dynamics simulations, two reaction pathways were identified and neither follows the mechanism for neutral guanosine. Singlet O_2 oxidation of protonated 9-methylguanine begins by a concerted cycloaddition; but it is mediated by a 5,8-endoperoxide. By contrast, a concerted cycloaddition does not occur for deprotonated 9-methylguanine. The latter involves a stepwise addition starting with the formation of an 8-peroxide, which subsequently evolves to a 4,8-endoperoxide. This dichotomy implies that acidic and basic media may lead to different chemistries for guanosine oxidation in aqueous solutions, starting from initial stage. The comparison with oxidation of protonated/deprotonated guanine illustrates the different mechanisms and products and particularly the suppressed oxidizability of 9-methylguanine *vs.* free guanine.

1 Introduction

Singlet O_2 is an electronically excited reactive oxygen species produced in biological systems.[1] It introduces oxidative stress in cells, leading to protein misfunctionality, mutagenic alterations to DNA, lipid peroxidation and membrane degradation. Guanine nucleobases have been shown to be the exclusive DNA target for $^1O_2$ attack. The corresponding process has been studied for three decades due to the roles of the guanine oxidation products in the processes of aging, photocleavage,

mutation, carcinogenesis and cellular death,[2–4] as well as in the photodynamic therapy for cancer.[5]

As shown in Scheme 1, $^1O_2$ oxidation of the 2′-deoxyguanosine (dGuo) moiety in DNA leads to the formation of 8-oxo-7,8-dihydro-2′-deoxyguanosine (8-oxodGuo) and its minor tautomer 7,8-dihydro-8-hydroxy-2′-deoxyguanosine (8-OHdGuo).[6] $^1O_2$ oxidation of dGuo as a free nucleoside or in short oligonucleotides, on the other hand, produces spiroiminodihydantoin-2′-deoxyribonucleoside (dSp) and guanidinohydantoin-2′-deoxyribonucleoside (dGh) with product branching being dependent on reaction conditions.[7–9] All of the processes have been assumed to be initiated by the formation of a 4,8-OO-dGuo endoperoxide *via* the Diels–Alder cycloaddition of $^1O_2$ to the imidazole ring.[10] This mechanism agrees with the origin of the inserted O atoms in the final products identified using ^{18}O-labeled mass spectrometric measurements.[7,8] However, the direct measurement of endoperoxide is challenging due to its instability and reactivity with water.[10–12] The most frequently cited experiment, from which the cycloaddition mechanism was extrapolated, is NMR characterization of photooxidation of

[a] *Department of Chemistry and Biochemistry, Queens College of the City University of New York, 65-30 Kissena Blvd., Queens, NY 11367, USA. E-mail: jianbo.liu@qc.cuny.edu*

[b] *Ph.D. Program in Chemistry, the Graduate Center of the City University of New York, New York, NY 10016, USA*

† Electronic supplementary information (ESI) available: Structures and Cartesian coordinates of all tautomers of 9MG, [9MG + H]⁺(H₂O)₀,₁ and [9MG−H]⁺(H₂O)₀,₁. Cartesian coordinates of the structures in Fig. 1, 3 and 4. Videos of the IRC trajectory of 5,8-OO-[9MG + H_N7]⁺ → TS2⁺ → TS3⁺ → TS4⁺ → 5-OH-8-oxo9MG⁺ in Fig. 1 and of the direct trajectory in Fig. 6. See DOI: 10.1039/c6cp01350c
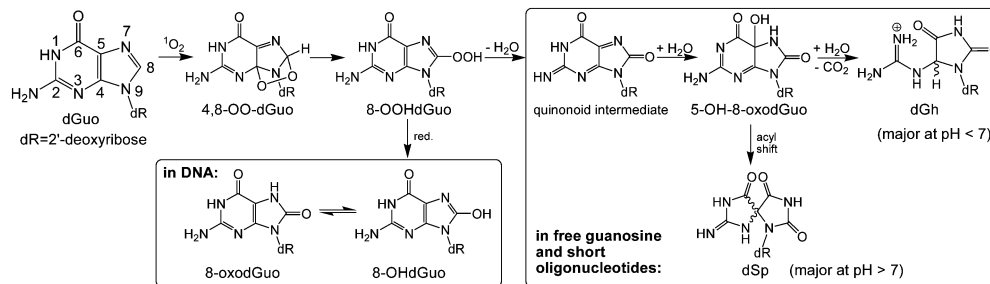
Scheme 1 $^1O_2$ oxidation of dGuo in aqueous solution. 8-oxodGuo may be oxidized to dSp by a second $^1O_2$.[6–9]

2′,3′,5′-*O*-(*tert*-butyldimethylsilyl)-8-methylguanosine in CD_2Cl_2 at −78 °C. The successful trapping of 8-methylguanosine endoperoxide is because the methyl substitution of C8-H reduced the reactivity of the ensuing endoperoxide. However, the 8-methyl-"capped" endoperoxide shut down the rearrangement to hydroperoxide, and decayed back to starting reactants *via* a retro Diels–Alder reaction when warmed to −30 °C.[10] For other guanosine derivatives where the labile 8-H is preserved, no endoperoxide could be detected even at −100 °C.[11] Mechanistically, it remains elusive whether the $^1O_2$ addition is concerted (*via* cycloaddition in unison) or stepwise (involving the formation of a terminal adduct first).[13,14]

Protonation and deprotonation of guanine bases through ionization[15–18] and/or intermolecular proton transfer within guanine–cytosine base pairs[19,20] represent another factor related to DNA damage due to mispairing of complementary bases and consequent genetic mutations.[21,22] Protonation and deprotonation of guanine also play a crucial role in enzymatic reactions and stabilization of triplex structures.[23] On the basis of the pK_{a1} (3.20, N7) and pK_{a2} (9.65, N1) of guanine, the population of deprotonated guanine is 0.2–2% in the range of pH 7–8[15]—a quite significant population. On the other hand, guanine is the most readily protonated nucleobase, due to its highest proton affinity among four bases. Understanding the oxidation of guanine in different ionization states and probing the synergistic effects when oxidation and ionization occur to the nucleobase at the same time will help further elucidate the oxidation consequences of DNA. However, except a few guanine photo-oxidation experiments in acidic and basic media,[24,25] no detailed investigation was available.

Recently, we reported the reactions of $^1O_2$ with mono-hydrated protonated ([G + H]$^+$(H$_2$O)) and deprotonated guanine ([G−H]$^-$(H$_2$O)) in the gas phase.[26] Transient intermediates were captured at room temperature using ion-molecule scattering mass spectrometry. Accompanying reaction potential energy surfaces (PESs), kinetic modeling and dynamics simulations supported a 5,8-endoperoxide structure for the intermediates detected in these reactions. This work has pieced together mechanisms, kinetics and dynamics concerning the early stage of $^1O_2$-induced guanine oxidation, which was missing from conventional condensed-phase studies. Nevertheless, guanine lacks the 2′-deoxyribose at N9, and thus may not be able to completely reproduce the oxidation chemistry of its nucleoside.

In this work, 9-methylguanine (9MG), a frequently used prototype substrate[27–32] of guanine nucleoside (where the sugar group is replaced by a methyl group), was adopted as a model system to bring our study a step closer than the guanine model[26] to the actual guanosine oxidation process. The point is to address synergistic effects between ionization, hydration and 9-substitution on guanine nucleoside oxidation. 9MG has the same protonation (N7) and deprotonation sites (N1 for monohydrated 9MG) as guanosine. The pK_a values are 3.11 (pK_{a1}) and 9.56 (pK_{a2}) for 9MG,[33] close to 2.20 and 9.50 for guanosine[34] and 2.30–2.85 and 9.99–10.18 for guanine bases in oligonucleotides.[35] For comparison, the ribose 2′,3′-diol only loses a proton above pH 12,[34,36] and cannot compete with deprotonation on guanine. IR–UV double resonance spectroscopy of hydrated clusters of guanosine and 9MG[30] revealed that the most stable mono-hydrated conformer of guanosine is analogous to that of 9MG, and their IR spectra correspond well. Munk *et al.*[29] reported that the different substituents at N9 had little effect on relative enthalpies of reactants, intermediates, transition states (TSs) and products for oxidative transformation of guanine. Therefore, the reductionist approach of using 9MG is reasonable in modeling the reaction coordinates of nucleoside oxidation.

Experiments were carried out using a guided-ion-beam tandem mass spectrometer.[37] 9MG was scattered from $^1O_2$ in different ionization and hydration states including protonated [9MG + H]$^+$(H$_2$O)$_{0,1}$ and deprotonated [9MG–H]$^-$(H$_2$O)$_{0,1}$. To eliminate radicals accompanying the photosensitized generation of $^1O_2$,[38] $^1O_2$ was produced by the reaction of H_2O_2 with Cl_2 in basic solution.[39,40] Experimental results were interpreted in light of molecular potential, kinetics and dynamics simulations. To this end, density functional theory (DFT), MP2 and CCSD(T) were employed to characterize reaction intermediates, TSs and products, and to simulate reaction kinetics and dynamics. We also used a multi-reference wavefunction methodology to examine the importance of non-dynamic electron correlation for reactions. On the basis of experimental and theoretical investigations, two oxidation pathways may be proposed: a concerted cycloaddition of O_2 to protonated 9MG across the C5–C8 bond, and a stepwise addition to deprotonated 9MG initiated by binding $^1O_2$ to C8 only. Neither follows Scheme 1. In addition, the comparison with guanine oxidation illustrates decreased oxidizability and different products induced by 9-methyl substitution.

15224 | *Phys. Chem. Chem. Phys.*, 2016, **18**, 15223–15234

This journal is © the Owner Societies 2016

2 Experimental and computational section

2.1 $^1O_2$ generation and detection

$^1O_2$ was generated by the reaction of $H_2O_2 + Cl_2 + 2KOH \rightarrow O_2$ ($\sim$85% $X^3\Sigma_g^-$ and $\sim$15% $a^1\Delta_g$) + 2KCl + $2H_2O$.[39,40] 10.5 mL of 8 M KOH was added to 20 mL of 35 wt% H_2O_2 in a sparger at -18 °C. The resulting mixture was degassed quickly. Immediately following degassing, 3.4 sccm of Cl_2 ($\geq$99.5%, Sigma-Aldrich) was mixed with 53.5 sccm of He and bubbled through the H_2O_2/KOH slush. All the Cl_2 reacted with H_2O_2. Gaseous products were passed through a cold trap (-70 °C) to remove water vapor. Only $^1O_2$, $^3O_2$ and He remained in the product gas.

The concentration of $^1O_2$ in the product gas was determined by measuring the $^1O_2$ emission ($a^1\Delta_g \rightarrow X^3\Sigma_g^-$, $\nu = 0$–0)[41] at 1270 nm in an optical emission cell. Emission from the cell was collected using a plano-convex lens, passed through an optical chopper (SRS model SR450) and a 1270 nm interference filter, and focused into a thermoelectrically cooled InGaAs detector (Newport model 71887) coupled with a lock-in amplifier (SRS model SR830). The amplifier output was converted to absolute $^1O_2$ concentration.[42] To reduce the residence time and therefore the wall- and self-quenching of $^1O_2$ within the $^1O_2$ chemical generator, the entire generator was continuously evacuated using a mechanical pump, and the pressure of the generator was maintained at 13 Torr through a pressure relay. The pump continuously removed the quenched O_2, so that maximum $^1O_2$ concentration was available for reaction with 9MG ions.

2.2 Ion-molecule reactions and mass spectrometric measurements

Reactions of 9MG ions with $^1O_2$ were carried out on a home-made guided-ion-beam tandem mass spectrometer.[37] The apparatus consists of an ion source, a radio frequency (f) hexapole ion guide, a quadrupole mass filter, an rf octopole ion guide surrounded by a scattering cell, second quadrupole mass filter, and a pulse-counting detector. Reactant ions were generated by electrospray ionization (ESI). A solution of $[9MG + H]^+$ was prepared in ethanol/water (2 : 1 v/v) containing a 0.5 mM mixture of 9MG ($\geq$98%, Aldrich) and HCl, and that of $[9MG–H]^-$ was prepared in ethanol/water (3 : 1) containing 0.5 mM 9MG and equimolar NaOH. The solution was electrosprayed in an ambient atmosphere at a flow rate of 0.05–0.06 mL h^{-1}, with the ESI potential set to 2.2 and -2.1 kV in positive and negative ion modes, respectively. Charged droplets were led into the source chamber through a desolvation capillary. The distance between the ESI emitter tip and the entrance of the capillary was 1.0 cm. The capillary was held at 100 V for positive ions and -90 V for the negative ones. The optimal temperature of the capillary was found to be 129–134 °C for $[9MG + H]^+$ and $[9MG–H]^-$, and 112 °C for their mono-hydrates.

A skimmer is located at the end of the source chamber. Ions were transported through the skimmer to the hexapole ion guide (maintained at a pressure of 24 mTorr), undergoing multiple collisions with background gas and thermalized to 310 K. Ions then passed into a conventional quadrupole mass filter for the selection of reactant ions. Reactant ions were focused into the octopole ion guide, which trapped ions in the radial direction, minimizing the loss of the reactant and product ions resulting from scattering. The octopole is surrounded by a scattering cell. The reactant gas from the $^1O_2$ generator was leaked into the scattering cell through a leak valve. The cell pressure was measured using a Baratron capacitance manometer (MKS 690 head and 670 signal conditioner). After passing through the scattering cell, the remaining reactant ions and product ions drifted to the end of the octopole, mass analyzed by the second quadrupole, and counted. The kinetic energy of reactant ions in the laboratory frame (E_{Lab}) was controlled by a DC bias voltage applied to the octopole. E_{Lab} can be converted into the E_{col} between ions and $^1O_2$ in the center-of-mass frame using $E_{col} = E_{Lab} \times m_{neutral}/(m_{ion} + m_{neutral})$ with $m_{neutral}$ and m_{ion} being the masses of neutral and ionic reactants, respectively. The initial kinetic energy of the ion beam was 0.9–1.0 eV, and the energy spread was 0.6 eV which resulted in 0.1 eV energy resolution for the collisions of $[9MG + H]^+(H_2O)_{0,1}/[9MG–H]^-(H_2O)_{0,1}$ with $^1O_2$. Reaction cross sections were calculated from the ratios of reactant and product ion intensities, the pressure of $^1O_2$ in the scattering cell (=cell pressure × the concentration of $^1O_2$), and the effective cell length. The cell pressure was set to 0.25 mTorr containing 6% of $^1O_2$/$^3O_2$ and 94% of He. Under these conditions, the reactant ions underwent at most a single collision with O_2. Ions also collided with He, but heavy ion–light neutral combination made these collisions insignificant.

To check the reactivity of reactant ions toward $^3O_2$/He, control experiments were performed under the same conditions except that Cl_2 used for the $^1O_2$ chemical generator was replaced by the $^3O_2$ gas at the same flow rate. Because the measured reaction cross sections are small, it was important to minimize the systematic variations under experimental conditions that might be caused by drifting potentials, changes in ion beam intensities, etc. In the experiments, we cycled through different E_{col} several times, and the kinetic energy of the primary ion beam was calibrated before and after each experiment. On the basis of the reproducibility in cross section measurements, we estimated that relative error is less than 25%.

2.3 Geometries, potential profiles and reaction coordinates

The electronic structures of reactants, intermediates, TSs and products were calculated using Gaussian 09 (rev. D.01).[43] The B3LYP method, with 6-31G*, 6-31+G*, 6-311++G** and aug-cc-pVQZ basis sets, was chosen for most calculations based on its reliable description of the $^1O_2$ oxidation of guanine,[26] 6-thioguanine[44] and histidine.[45] Restricted-to-unrestricted instabilities were checked. For those without stable wavefunctions in restricted calculations, unrestricted methods were used, and spin contamination was not an issue. Energies of intermediates were refined at the CCSD(T)/6-31+G* level using B3LYP/6-31+G* geometries. To ascertain that CCSD(T)//B3LYP calculations might be invalidated by multi-reference effects, CASSCF(10,8) and T1 diagnostic[46] were performed for critical structures. For the reactions of deprotonated 9MG, a composite CASMP2/6-311++G**//CASSCF(10,8)/6-31+G* approach was used in addition to the DFT method, aimed at assessing the importance of non-dynamical electron correlation.

The active space consisted of those orbitals involved in forming 8-peroxide and endoperoxide.

Tautomer/rotamer search was conducted for reactants, and their most stable structures were used in PES, RRKM[47] and direct dynamics trajectory calculations. Each TS was verified as first-order saddle points. IRC calculation was carried out to determine whether the TS is located between the correct energy minima. DFT-calculated vibrational frequencies and zero-point energies (ZPEs) were scaled by factors of 0.968 and 0.988,[48] respectively. Energies were corrected for by including thermal corrections at 298 K. RRKM rate constants were calculated using the program of Zhu and Hase,[49] using a direct state count algorithm.

2.4 Direct dynamics trajectory simulations

Trajectories for the collisions of $[9MG–H_{N1}]^-(H_2O) + {}^1O_2$ at $E_{col} = 0.1$ eV were simulated using Venus[50] interfaced with Gaussian 09. To select a suitable level of theory for trajectory integration, we performed relaxed PES scans for the approach of ${}^1O_2$ to $[9MG–H_{N1}]^-(H_2O)$ using various DFT methods, and compare these results to the benchmark PES using CASSCF(10,8)/6-31+G*. On the basis of the overall level of accuracy and computational cost, B3LYP/6-31G* was chosen. We found that the polarization function is necessary to achieve the correct geometry of the O_2 moiety. Trajectories were initiated at a separation between collision partners of 8.0 Å, with a collision impact parameter of 0 Å. Vibrational and rotational temperatures of reactants were set to 300 K, to mimic the ion-beam experiment. Quasi-classical Boltzmann sampling was used to select vibrational and rotational energies. Each molecule had ZPE in all vibrational modes. E_{col} was added as relative translation energy.

The Hessian-based predictor-corrector algorithm[51] was used for the numerical integration of the classical equations of motion, with the Hessian updated every five steps. The integration step size was 0.25 amu$^{1/2}$ Bohr, corresponding to a step size of 0.5–0.6 fs in trajectory time. The total energy of the system was conserved (within an uncertainty of 10^{-4} Hartree) and the system remained in the singlet electronic state. A quadratically convergent SCF method was used for trajectory integration in case the first-order SCF algorithm failed to converge within allotted cycles. Trajectories were terminated when the product separation exceeded 8.1 Å. A total of 100 trajectories were completed, each taking 300–400 CPU hours on an Intel 32-core based computational cluster.

3 Results and discussion

3.1 Addition of ${}^1O_2$ to protonated 9MG is concerted, but leads to a 5,8-endoperoxide

The structures of neutral, protonated and deprotonated 9MG as well as their mono-hydrates are provided in Fig. S1–S5 (ESI†). All of these structures were calculated at the B3LYP/6-311++G** level of theory. Their Cartesian coordinates are reported in the ESI.† The global minima are summarized in Scheme 2. The most stable $[9MG + H]^+$ is formed by protonation of the N7 of neutral 1H-keto-9MG, and the most stable $[9MG–H]^-$ is formed by deprotonating an N10-H of 1H-ketone. Hydration energies of ions were calculated using $E_{hydration} = E(\text{bare ion}) + E(H_2O) - E(\text{cluster})$, with $E(\text{bare ion})$, $E(H_2O)$ and $E(\text{cluster})$ being the energies of the bare ion, water and the hydrate of the same ion tautomer, respectively. The most favorable hydration motif is formed by a water hydrogen-bonded to both C6-carbonyl and N7H (or N7) concurrently. Interestingly, after addition of an explicit water ligand the N1-H of 1H-ketone becomes the most acidic site (as in aqueous solution[52]). We included protonation/deprotonation sites in the notations of the lowest-lying $[9MG + H_{N7}]^+(H_2O)_{0,1}$, $[9MG–H_{N10}]^-$ and $[9MG–H_{N1}]^-(H_2O)$. These species were dominating in the corresponding gas-phase reactions with ${}^1O_2$ due to their populations at 298 K.

We started by first measuring the reactions of ${}^1O_2$ with bare and mono-hydrated $[9MG + H_{N7}]^+$ over an E_{col} range of 0.1–1.0 eV. To guide the interpretation of experimental results, the PESs for $[9MG + H_{N7}]^+(H_2O)_{0,1} + {}^1O_2$ were modeled at the B3LYP/6-31+G* level (Fig. 1). Potential energies were refined by single-point calculations at the CCSD(T)/6-31+G* level using B3LYP optimized geometries. To ascertain that the CCSD(T)// B3LYP calculations might be invalidated by multi-reference effects, CASSCF(10,8)/6-31+G* and T1 diagnostic of Lee[46] were performed for the structures along the reaction coordinates. In most cases, the coefficient of the Hartree–Fock configuration exceeds 0.95, and the T1 value derived from CCSD(T) is below or close to the upper limit (0.02, above which non-dynamic correlation effects may be large enough to make the single-reference method unreliable), except for 8-OO$[9MG + H_{N7}]^+$ in which T1 is up to 0.04. However, 8-OO$[9MG + H_{N7}]^+$ was inaccessible in the experiment due to its high energetics. Also note that CCSD(T) with the inclusion of perturbative correction for triplet excitation may be able to compensate the deficiencies of a single-determinant reference, as found in the CCSD(T)// B3LYP study of ${}^1O_2$ addition to histidine[45] and alkenes.[53]
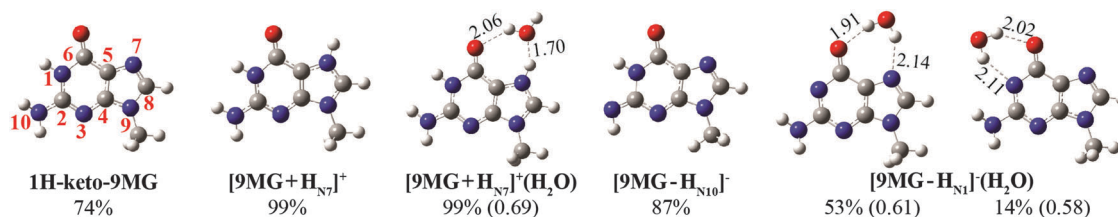
Scheme 2 B3LYP/6-311++G** calculated lowest-lying tautomers of 9MG, $[9MG + H]^+(H_2O)_{0,1}$ and $[9MG–H]^-(H_2O)_{0,1}$, with abundances at 298 K. Numbering scheme and nomenclatures are presented. Dashed lines indicate hydrogen bonds. Bond lengths are shown in Å. Hydration energies (eV) are indicated in parentheses.
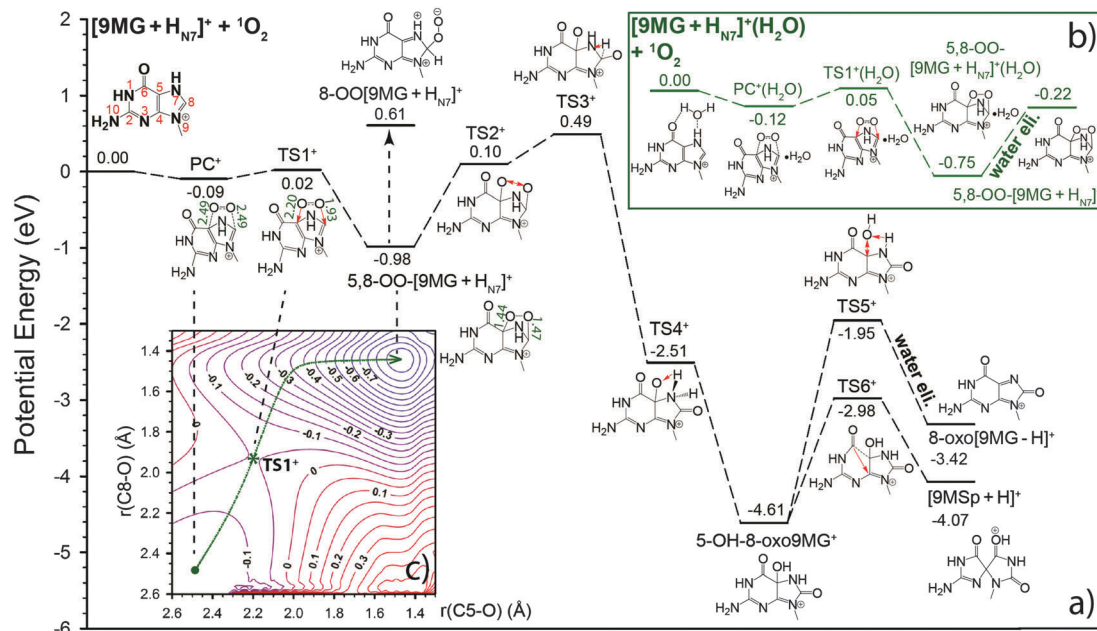
15226 | Phys. Chem. Chem. Phys., 2016, 18, 15223–15234

This journal is © the Owner Societies 2016

Fig. 1 Reaction coordinates for (a) [9MG + H$_{N7}$]$^+$ + ^{1}O$_2$ and (b) [9MG + H$_{N7}$]$^+$(H$_2$O) + ^{1}O$_2$. Energies (eV, relative to reactants) were evaluated based on the sum of electronic energies calculated at the CCSD(T)/6-31+G*//B3LYP/6-31+G* level and thermal corrections (298 K) at the B3LYP/6-31+G* level. For TSs, vibrational modes corresponding to imaginary frequencies are indicated by red displacement vectors. (c) Relaxed 2D PES for the cycloaddition of ^{1}O$_2$ to the C5 and C8 of [9MG + H$_{N7}$]$^+$. Numbers in the contour map are potential energies calculated at the B3LYP/6-31+G* level. Green line represents an IRC trajectory.

Therefore, the CCSD(T)//B3LYP combination is expected to be appropriate for reproducing the mechanism for the early stage of [9MG + H$_{N7}$]$^+$ oxidation.

The reaction of [9MG + H$_{N7}$]$^+$ first forms a reactant-like precursor complex PC$^+$ which evolves to a bicyclic endoperoxide through a [4+2] cycloaddition at TS1$^+$. An intriguing result is that the cycloaddition gives rise to a 5,8-OO-[9MG + H$_{N7}$]$^+$. This contrasts with the structure of 4,8-endoperoxide that was proposed to be the intermediate for ^{1}O$_2$ oxidation of neutral guanosine.[6,7,10] We explored the possibility of cycloaddition of ^{1}O$_2$ to the C4 and C8 positions of [9MG + H$_{N7}$]$^+$ by running a relaxed PES scan along the approach of one end of O$_2$ toward C4. However, the PES avoided a 4,8-endoperoxide structure but converged to a 5,8-endoperoxide.

To further verify that the ^{1}O$_2$ addition to [9MG + H$_{N7}$]$^+$ follows a concerted cycloaddition but not a stepwise mechanism,[54] a 27 × 27 grid of potential surface for governing the addition was generated at the B3LYP/6-31+G* level using a relaxed PES scan, and is visualized in Fig. 1c. Two geometrical parameters r(C5-O) and r(C8-O), which characterize the distance between the imidazole ring and the O$_2$ moiety, are considered as reaction coordinates and each decreased from 2.6 to 1.3 Å at an interval of 0.05 Å. All the other bond lengths and angles were optimized at each point of the PES. On this PES, there is a deep well corresponding to 5,8-OO-[9MG + H$_{N7}$]$^+$ which is separated from PC$^+$ by a saddle point located at TS1$^+$. A minimum energy pathway along the intrinsic reaction coordinate, i.e. IRC trajectory, is projected onto the PES, giving an intuitive picture of the reaction. The IRC trajectory features a synchronous attack of ^{1}O$_2$ on the imidazole ring and nearly

symmetric distances of r(C5-O) and r(C8-O) when moving through TS1$^+$ toward the product.

5,8-OO-[9MG + H$_{N7}$]$^+$ may evolve to form 5-OH-8-oxo9MG$^+$ (i.e. protonated 5-hydroxy-7,8-dihydro-9-methylguanine) through TS2$^+$ (homolytic cleavage of the dioxo bridge), TS3$^+$ (intramolecular H transfer from C8 to N7) and TS4$^+$ (subsequent H transfer from N7 to C5-O). A video of the IRC trajectory crossing TS2$^+$, TS3$^+$ and TS4$^+$ is available in the ESI.† The reaction enthalpy (ΔH_{rx}) for 5-OH-8-oxo9MG$^+$ is −4.61 eV, but the TSs amount to a 0.49 eV barrier. While this rearrangement seems similar to the formation of 5-OH-8-oxodGuo from 4,8-OO-dGuo at neutral pH (see Scheme 1), differences are notable due to the different starting endoperoxides (i.e. 5,8-OO- vs. 4,8-OO-endoperoxide). First, the formation of 5-OH-8-oxo9MG$^+$ from 5,8-OO-[9MG + H$_{N7}$]$^+$ involves three adjacent TSs but no intervening intermediates. By contrast, the rearrangement from 4,8-OO-dGuo to 5-OH-8-oxodGuO needs to be mediated by two intermediates—an 8-OOHdGuo and a quinonoid intermediate. Secondly, as opposed to the transformation of 5,8-OO-[9MG + H$_{N7}$]$^+$ → 5-OH-8-oxo9MG$^+$ where no reactive or catalytic water is needed, addition of an explicit water ligand to the quinonoid is required for transformation into 5-OH-8-oxodGuO.[7,8] These differences may imply the influence of nucleoside protonation on its oxidation pathway and the fate of the intermediates.

The PES also suggests that ensuing 5-OH-8-oxo9MG$^+$ may eliminate a water molecule from C5–N7 (TS5$^+$), producing 8-oxo[9MG–H]$^+$; or rearranges to [9MSp + H]$^+$ via an acyl shift (TS6$^+$). In addition, following a similar pathway to 5-OH-8-oxoG$^+$ → [Gh + H]$^+$ proposed in a previous study,[55] 5-OH-8-oxo9MG$^+$ may

This journal is © the Owner Societies 2016

Phys. Chem. Chem. Phys., 2016, 18, 15223–15234 | 15227

interconvert to $[9MGh + H]^+$. Note that 5,8-OO-$[9MG + H_{N7}]^+$ may also interconvert to a linear 8-OO$[9MG + H_{N7}]^+$, from which a 8-hydroperoxy intermediate 8-OOH9MG$^+$ might be expected. But high reaction energetics renders the formation of 8-OO$[9MG + H_{N7}]^+$ mechanistically insignificant. Therefore, this species is not considered further.

Of all the intermediates, only 5,8-OO-$[9MG + H_{N7}]^+$ has favorable energetics and is expected to be the dominant product at low E_{col}. However, this intermediate was not present in product mass spectra. We have employed RRKM[47] theory to model individual dissociation steps leading from 5,8-OO-$[9MG + H_{N7}]^+$. At low E_{col}, only one channel was appreciable, that is decay back to reactants. This accounts for the lifetime (< 200 μs) of 5,8-OO-$[9MG + H_{N7}]^+$ at $E_{col} < 0.2$ eV. However, this lifetime was much shorter compared to the time-of-flight of product ions (i.e. 400–500 μs) through the octopole ion guide and the second quadrupole of the tandem mass spectrometer. As a result, 5,8-OO-$[9MG + H_{N7}]^+$ was determinedly to decay back to reactants before reaching the ion detector.

To capture transient 5,8-OO-$[9MG + H_{N7}]^+$ in mass spectra, we devised a reaction route by using $[9MG + H_{N7}]^+(H_2O)$ (m/z 184) as the target ion for collision with $^1O_2$. The strategy is to stabilize nascent endoperoxide based on water evaporation cooling of gas-phase hydrate.[26,56] We have used this strategy to capture endoperoxides in the reactions of $^1O_2$ with guanine[26] and histidine.[56] Only one primary product (m/z 198) was observed for $[9MG + H_{N7}]^+(H_2O) + {}^1O_2$, corresponding to the liberation of a water molecule from the O_2 adduct. The corresponding PES is illustrated in Fig. 1b. The driving force for this product channel came from the ejection of the water ligand from 5,8-OO-$[9MG + H_{N7}]^+(H_2O)$. The water dissociation energy is 0.53 eV, less than the threshold of 0.80 eV for a retro-Diels–Alder reaction of 5,8-OO-$[9MG + H_{N7}]^+$. Elimination of water and the accompanying product kinetic energy release removed the heat of endoperoxide formation carried by nascent 5,8-OO-$[9MG + H_{N7}]^+$ that would otherwise prompt its decomposition. In our experiment, the reaction was limited to the formation of 5,8-OO-$[9MG + H_{N7}]^+$ because forming downstream products must overcome a barrier of a half eV above reactants.

Fig. 2a shows the integral cross section ($\sigma_{reaction}$) for $[9MG + H_{N7}]^+(H_2O) + {}^1O_2$ and the reaction efficiency ($= \sigma_{reaction}/\sigma_{collision}$, with $\sigma_{collision}$ being the greater of ion-induced dipole capture cross section[57] and hard-sphere collision cross section). Error bars were estimated by the variations between multiple data sets, with relative uncertainties of $\sim 25\%$. The rise of cross section and efficiency at 0.5 eV is likely an artifact due to the uncertainty in measurements. The efficiencies at the high E_{col} range were not plotted as the values are too small to allow for a meaningful comparison. We state that the absolute uncertainties in the cross sections and efficiencies, arising largely from ion collection and detection efficiencies and absolute $^1O_2$ concentrations, could be larger than the indicated error bars. However, these sources of uncertainties would not affect relative cross sections, i.e., their E_{col} dependence which is our primary interest here.

A key feature in understanding ion-molecule reactions is whether reactions are exothermic or endothermic. In other
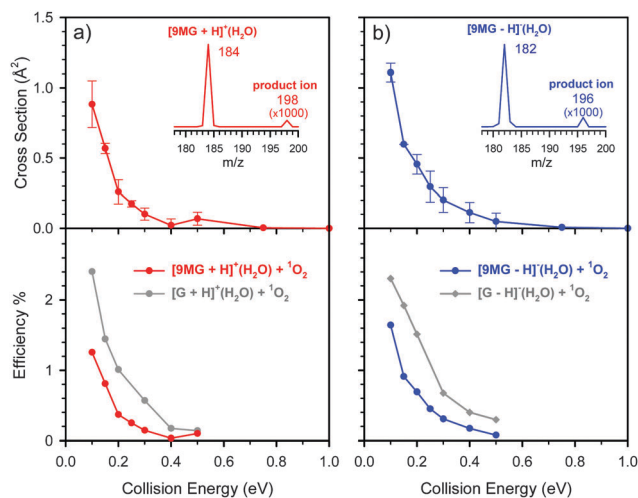

Fig. 2 Reaction cross sections and efficiencies for $^1O_2$ oxidation of (a) $[9MG + H_{N7}]^+(H_2O)$ and (b) $[9MG-H_{N1}]^-(H_2O)$. Insets show product mass spectra measured at $E_{col} = 0.1$ eV. Reaction efficiencies of hydrated protonated and deprotonated guanine[26] are presented for comparison.

words, if they require energy in overcoming the activation barriers to products.[58] Clearly, the reaction of $[9MG + H_{N7}]^+(H_2O) + {}^1O_2$ exhibits no barriers to the formation of products. As for any exothermic process, the reaction efficiency is significant only at the lowest E_{col} (albeit it is only 1.5% or less at 0.1 eV). Increasing the amount of energy available decreased the probability of the reaction; as a consequence, the efficiency decreases rapidly at higher E_{col}, eventually becoming zero at the collision energy above 0.5 eV. A similar E_{col} dependence was observed for the $^1O_2$ oxidation of $[9MG-H_{N1}]^-(H_2O)$ and of protonated and deprotonated guanine which are included in Fig. 2 and will be discussed later.

To the best of our knowledge, there was no experimental assessment of the activation barriers associated with the initial stage of the $^1O_2$ oxidation of guanine and guanosine. Previous calculations for neutral 9MG + $^1O_2$ suggested an initial activation barrier of 0.87 eV above the starting reactants.[14] The E_{col} dependence of reaction cross sections measured in our ion-beam experiments confirmed that the initial oxidation of hydrated $[9MG + H_{N7}]^+$ (and $[9MG-H_{N1}]^-$ to be discussed below) has no barriers above reactants and is sufficiently exothermic that it is possible to eliminate the water ligand from the reacting complexes. These experimental data serve as a critical benchmark for our CCSD(T)//B3LYP calculation of reaction PESs.

3.2 $^1O_2$ addition to deprotonated 9MG occurs stepwise

Reaction in the absence of water. According to the B3LYP/6-31+G* predicted PES (Fig. 3a), the lowest energy deprotonated tautomer $[9MG-H_{N10}]^-$ could not undergo a Diels–Alder cycloaddition with $^1O_2$, presumably because the C4–C5 ethylenic bond delocalizes upon N10–H deprotonation. This is supported by a 0.01 Å increase in r(C4–C5) and meanwhile a 0.02 Å decrease in r(N3–C4) and a 0.01 Å decrease in r(C5–C6) of $[9MG-H_{N10}]^-$ compared to neutral $1H$-keto-9MG. As shown in Fig. 3a, $^1O_2$ attacks the C8 terminus of $[9MG-H_{N10}]^-$, producing

15228 | Phys. Chem. Chem. Phys., 2016, 18, 15223–15234

This journal is © the Owner Societies 2016

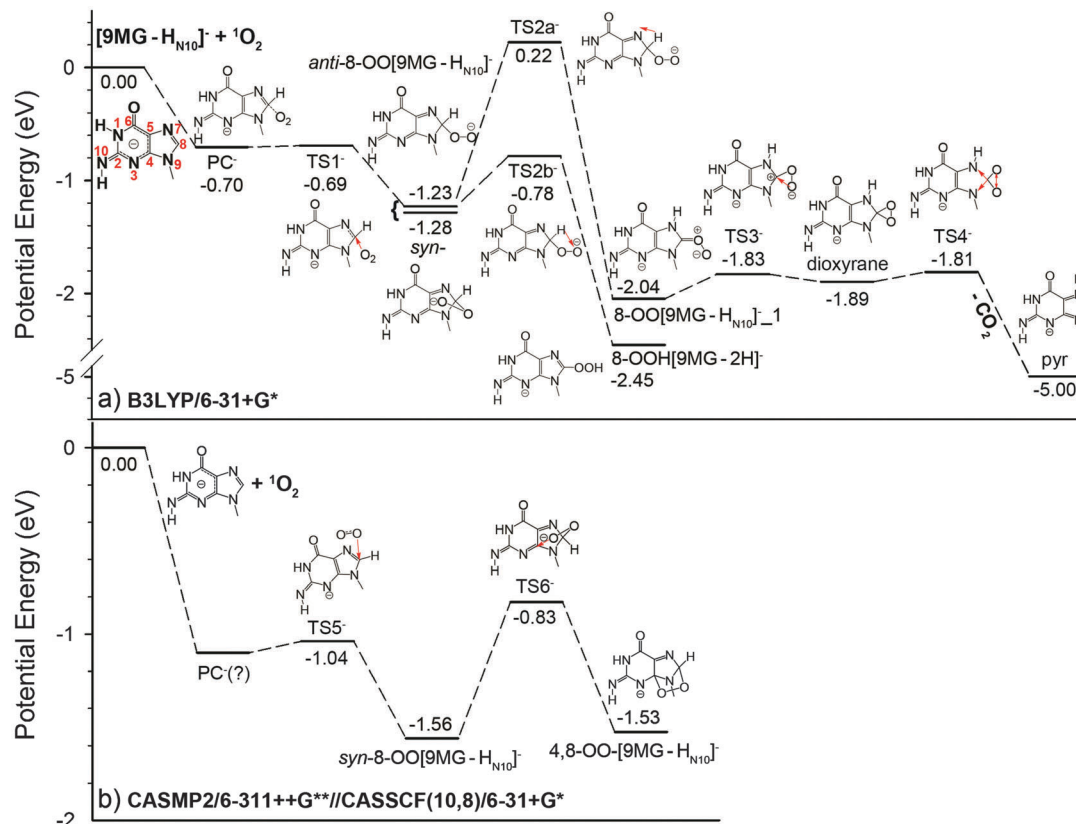**Fig. 3** (a) Reaction coordinate for $[9MG–H_{N10}]^- + {}^1O_2$. Energies (with respect to reactants) were calculated at the B3LYP/6-31+G* level, including thermal corrections at 298 K. (b) Stepwise formation of a 4,8-endoperoxide, deduced from CASMP2/6-311++G**//CAS(10,8)/6-31+G* calculations. For TSs, vibrational modes corresponding to imaginary frequencies are indicated by red displacement vectors.

an 8-OO$[9MG–H_{N10}]^-$ in an *anti-* or *syn-*configuration. Note that ${}^1O_2$ has been shown to be generally electrophilic, but it also has some nucleophilic character due to a high-lying HOMO.[45]

8-OO$[9MG–H_{N10}]^-$ may undergo intramolecular hydrogen transfer to 8-OO$[9MG–H_{N10}]^-$_1 via TS2a$^-$, or 8-OOH$[9MG–2H]^-$ via TS2b$^-$. 8-OO$[9MG–H_{N10}]^-$_1 may produce an 8C-dioxyrane anion which in turn breaks the imidazole ring at N7–C8 with concomitant liberation of CO_2, producing a pyrimidine-like product ion. The release of 8-CO_2 was observed in low-temperature (−78 to −100 °C) photosensitized oxidation of 2′,3′,5′-O-*tert*-butyldimethylsilyl-N-*tert*-butyldimethylsilyl-8-^{13}C-guanosine[11] and 2′,3′,5′-O-*tert*-butyldimethylsilylguanosine[12] in nonpolar organic solvents, with products being proposed as dioxyrane.

There are two issues with using DFT for the construction of reaction PES: (1) overstabilization of a charge-separated species, combined with a lack of intramolecular dispersion, may overestimate the stability of 8-OO$[9MG–H_{N10}]^-$;[13] (2) on the other hand, the source of error in the electron correlation associated with short interoxygen distance may underestimate the stability of endoperoxide.[13] To gauge the B3LYP results, we have explored the PES for $[9MG–H_{N10}]^- + {}^1O_2$ using a composite multi-referential approach CASMP2/6-311++G**//CASSCF(10,8)/6-31+G* with a second-order perturbation correction added to wavefunction.

It turns out that the B3LYP predicted stationary points and TSs in Fig. 3a could all be reproduced at the CASMP2//CASSCF level.

The overall profile obtained from the CASMP2//CASSCF PES is similar to that from B3LYP, with the discrepancies being the 4,8-OO-$[9MG–H_{N10}]^-$ and related TSs obtained from new calculations as summarized in Fig. 3b. At the CASMP2//CASSCF level, 4,8-OO-$[9MG–H_{N10}]^-$ becomes a stable intermediate and is formed by two steps. In the first step, ${}^1O_2$ approaches the C8 of $[9MG–H_{N10}]^-$ at TS5$^-$. r(C8–O) of TS5$^-$ is reduced to 1.79 Å, while the other O atom is located 2.48 Å away from C4, indicative of an asymmetric TS. Once forming *syn*-8-OO-$[9MG–H_{N10}]^-$, r(C8–O) and r(C4–O) become 1.33 Å and 3.15 Å, respectively. An attempt was made to locate a precursor complex between reactants and TS5$^-$, but all different starting geometries converged to *syn*-8-OO$[9MG–H_{N10}]^-$. This indicates that a precursor, if exists, must be located in a flat region on the CASSCF PES. In the second step, r(C4–O) is shortened to 1.94 Å whereas r(C8–O) is elongated to 1.40 Å at TS6$^-$, and they finally reach the equilibrium distances of 1.42 and 1.50 Å, respectively, in 4,8-OO-$[9MG–H_{N10}]^-$. To sum up, CASSCF calculations suggest a second pathway for $[9MG–H_{N10}]^- + {}^1O_2$—that is an asynchronous Diels–Alder leading to the formation of 4,8-OO-$[9MG–H_{N10}]^-$—with the second step being rate-limiting and the ΔH_{rx} is −1.53 eV. No concerted cycloaddition pathway could be located at CASSCF. As an additional note, TS5$^-$ becomes a high-order saddle point and 4,8-OO-$[9MG–H_{N10}]^-$ converges to *syn*-8-OO$[9MG–H_{N10}]^-$ at B3LYP.

This journal is © the Owner Societies 2016

Phys. Chem. Chem. Phys., 2016, **18**, 15223–15234 | **15229**

According to the RRKM analysis of both B3LYP and CASMP2//CASSCF PESs, 8-OO[9MG–H$_{N10}$]$^-$ and 8-OOH[9MG–2H]$^-$ (and possibly 4,8-OO-[9MG–H$_{N10}$]$^-$) all correspond to dead-end pathways which decomposed into reactants during their flight within the mass spectrometer. Consequently, as what we found for the reaction of dry [9MG + H$_{N7}$]$^+$, no product ions were detected for [9MG–H$_{N10}$]$^-$. Note that the electron detachment energy for [9MG–H]$^-$ tautomers was calculated to be 2.7–2.86 eV, which is beyond the maximum experimental E_{col}. Therefore, electron detachment from reactant ions could be disregarded in ion–molecule collisions. The charge transfer of [9MG–H]$^-$ + ^{1}O$_2$ → [9MG–H] + O$_2$$^-$ is endothermic by 1.27–1.43 eV, and thus could not occur in the experiment, either.

Changes upon the addition of an explicit water ligand. While the [9MG–H$_{N1}$]$^-$ tautomer accounts for only 13% of deprotonated 9MG in the gas phase, it becomes the dominant deprotonated structure in aqueous solution[52] and is therefore more biologically relevant. Experimentally, inclusion of an explicit water ligand shifts the favorable deprotonation site of 9MG from N10 to N1, yielding [9MG–H$_{N1}$]$^-$(H$_2$O) as the global minimum. The latter has two conformations (differing in water binding positions, Scheme 2), which account for a total of 67% of mono-hydrate at 298 K (for comparison, the population of [9MG–H$_{N10}$]$^-$(H$_2$O) drops to 31%). The experiment of mono-hydrated deprotonated 9MG thus provided a better platform for mimicking guanosine oxidation in basic solution.

Similar to the ^{1}O$_2$ addition/water elimination reaction scheme for [9MG + H$_{N7}$]$^+$(H$_2$O), the oxidation of [9MG–H$_{N1}$]$^-$(H$_2$O) (m/z 182) is able to form a stable product ion at m/z 196, accompanied by the elimination of water. The reaction cross section and efficiency are shown in Fig. 2b over the E_{col} range from 0.1 to 1.0 eV, along with the data for the reaction of [G – H]$^-$(H$_2$O) + ^{1}O$_2$ for comparison.[26] The reaction efficiency of [9MG–H$_{N1}$]$^-$(H$_2$O) is comparable to its protonated counterpart, and is strongly suppressed by E_{col}, becoming negligible at E_{col} > 0.5 eV. Again, such E_{col} dependence indicates that the reaction is exothermic and may proceed without barriers in excess of reactants.

The PES for [9MG–H$_{N1}$]$^-$(H$_2$O) + ^{1}O$_2$ is depicted in Fig. 4. Similar to that of [9MG–H$_{N10}$]$^-$, the reaction of [9MG–H$_{N1}$]$^-$(H$_2$O) may form an anti-8-OO[9MG–H$_{N1}$]$^-$(H$_2$O) through TS7$^-$(H$_2$O), and the barrier height is nearly equal to the precursor. Anti-8-OO[9MG–H$_{N1}$]$^-$(H$_2$O) may interconvert to its syn-rotamer. The PES also identified a 4,8-OO-[9MG–H$_{N1}$]$^-$(H$_2$O), which may form from syn-8-OO[9MG–H$_{N1}$]$^-$ via TS8$^-$(H$_2$O). Different from the reaction schemes proposed for neutral dGuo and [9MG–H$_{N10}$]$^-$ where an 8-OOHdGuo (Scheme 1) or 8-OOH[9MG–2H]$^-$ (Fig. 3a) may form from rearrangement of an intermediate, neither 8-OO[9MG–H$_{N1}$]$^-$ nor 4,8-OO-[9MG–H$_{N1}$]$^-$ is able to evolve to an 8-hydroperoxide. In fact, a putative 8-OOH[9MG–2H]$^-$ structure would eliminate an OH$^-$ (or •OH), producing a neutral 8-oxo[9MG–H$_{N1}$] (or 8-oxo[9MG–H$_{N1}$]•$^-$ radical). This suffices another piece of evidence showing the influence of nucleoside ionization and solvation on its oxidation.

According to PES analysis, both 8-OO[9MG–H$_{N1}$]$^-$ and 4,8-OO-[9MG–H$_{N1}$]$^-$ represent energetically favorable products for [9MG–H$_{N1}$]$^-$(H$_2$O) + ^{1}O$_2$. A question arises—which one dominated the reaction? Two efforts were made in an attempt to answer this question.

(i) A close look at 2D PES of ^{1}O$_2$ addition. Our first effort was to map out the 2D PES for the ^{1}O$_2$ addition to [9MG–H$_{N1}$]$^-$. To determine what accessible level of theory would provide a reasonably accurate picture of the reaction, DFT, MP2 and CASSCF methods were applied. The first row of Fig. 5 shows three surfaces obtained from UB3LYP, M06-2X and UωB97XD, respectively, all employing the 6-31+G* basis set. The three functionals range from the hybrid GGA to the hybrid meta-GGA and then to RSH, with a hope of an improvement in the prediction of the stability of 4,8-OO-[9MG–H$_{N1}$]$^-$ vs. 8-OO[9MG–H$_{N1}$]$^-$ when moving from the hybrid GGA to RSH.[13] The second row of Fig. 5 shows the surfaces derived from MP2 and CASSCF(10,8), using the 6-31+G* and 6-31G* basis sets, respectively.

Three DFT-derived surfaces present similar geometric features: (1) there are two product minima: one corresponds
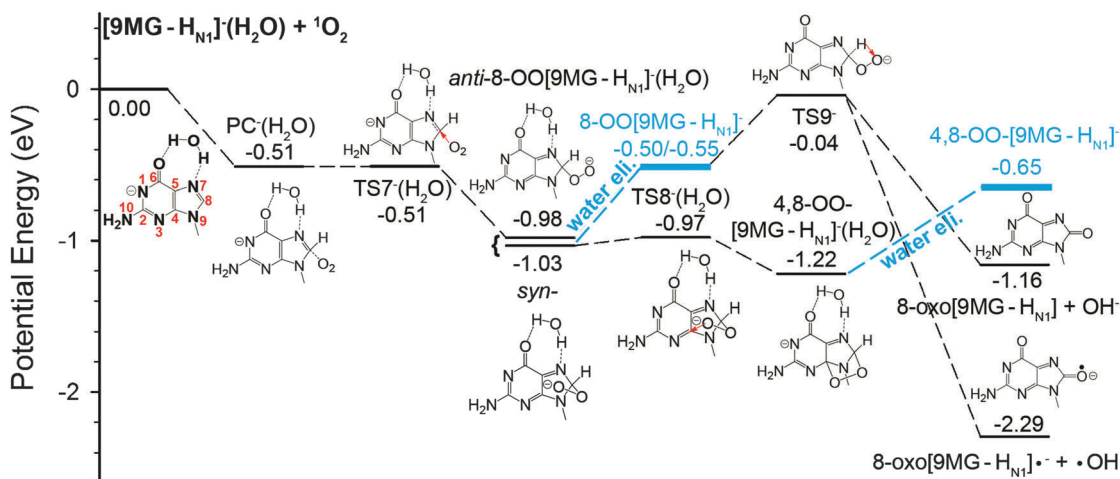

Fig. 4 Reaction coordinate for [9MG–H$_{N1}$]$^-$(H$_2$O) + ^{1}O$_2$. Energies are derived from a combination of B3LYP/6-31+G* and CCSD(T)/6-31+G* values, including thermal corrections (298 K). For TSs, vibrational modes corresponding to imaginary frequencies are indicated by red displacement vectors.
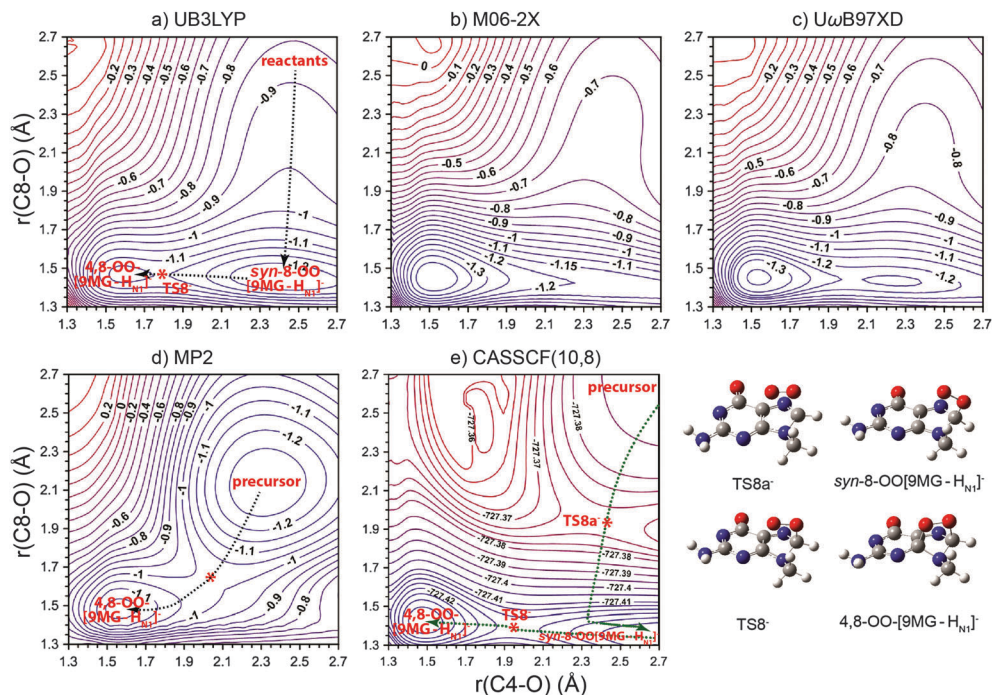
15230 | *Phys. Chem. Chem. Phys.*, 2016, **18**, 15223–15234

This journal is © the Owner Societies 2016

Fig. 5 PES scans along the addition of $^1O_2$ to [9MG–H_{N1}]$^-$, calculated at various levels of theory with the 6-31+G* basis set for (a–d) and 6-31G* for (e). Numbers in maps are potential energies (eV, relative to reactants), except for (e) where absolute electronic energies (Hartree) are used.

to 4,8-OO-[9MG–H_{N1}]$^-$ and the other corresponds to 8-OO[9MG–H_{N1}]$^-$, two of which are separated by a saddle point TS8$^-$. 8-OO[9MG–H_{N1}]$^-$ is in the *syn*-configuration owing to subsequent ring-closure constraints. Note that at M06-2X, the energy of *syn*-8-OO[9MG–H_{N1}]$^-$ increases slightly, diminishing the barrier to 4,8-OO-[9MG–H_{N1}]$^-$; (2) all three surfaces present a descending path for the formation of *syn*-8-OO[9MG–H_{N1}]$^-$ from reactants without a saddle point. This is because the "would-be" barrier (see TS7$^-$ in Fig. 4) is extremely flat at DFT levels. The dotted line on the B3LYP map represents a typical minimum energy path connecting reactants to 4,8-OO-[9MG–H_{N1}]$^-$ *via* *syn*-8-OO[9MG–H_{N1}]$^-$; (3) we have compared the surfaces constructed both in the presence and in the absence of the water ligand, using all three density functionals. No difference was observed; and (4) we have calculated a PES using the restricted B3LYP method, which yielded an identical landscape as UB3LYP.

In contrast to the two-step addition deduced from DFT, the exploration of the surface at the MP2 level predicts a concerted [4+2] cycloaddition. It features a tight precursor at r(C4-O) = 2.3 Å and r(C8-O) = 2.15 Å which leads to the formation of 4,8-OO-[9MG–H_{N1}]$^-$ (the only product formed on the MP2 PES) through a saddle point located at r(C4-O) = 2.0 Å and r(C8-O) = 1.65 Å. The MP2 theory fails to locate an 8-OO[9MG–H_{N1}]$^-$.

Apparently, the contrasting DFT and MP2 surfaces add up to a mechanistic paradox. As a resolution to this paradox, laborious computation was made to map out the surface at the CASSCF(10,8)/6-31G* level. The three potential wells located on the CASSCF surface correspond to the precursors, *syn*-8-OO[9MG–H_{N1}]$^-$ and 4,8-OO-[9MG–H_{N1}]$^-$, respectively. Two saddle points, TS8a$^-$ and TS8$^-$, were identified between the precursor and products.

TS8a$^-$, TS8$^-$, *syn*-8-OO[9MG–H_{N1}]$^-$ and 4,8-OO-[9MG–H_{N1}]$^-$ are located at 0.42, −0.74, −1.00, and −1.09 eV with respect to the precursor, respectively. There is a high-lying valley on the top left of the PES, which represents a strained structure due to specific r(C4-O) and r(C8-O) values in this region. The corresponding structure has the O_2 moiety bonded to C5 and lies at the energy of 0.61 eV above the precursor, rendering it mechanistically and energetically insignificant.

Of all the methods, B3LYP most closely reproduces the CASSCF potential landscape. The B3LYP predicted that reactants → *syn*-8-OO[9MG–H_{N1}]$^-$ → TS8$^-$ → 4,8-OO-[9MG–H_{N1}]$^-$ are in the same direction as that expected from the CASSCF surface. As to the difference between B3LYP and CASSCF, a saddle point TS8a$^-$ arises between reactants and *syn*-8-OO[9MG–H_{N1}]$^-$ on the CASSCF surface. Therefore, the two-step route has to be revised to include TS8a$^-$. The emergence of TS8a$^-$ on the CASSCF PES brings about a geometric feature, referred to as the valley-ridge inflection (VRI) point[53,59,60] on the downhill way from TS8a$^-$ to products. That is, the reaction pathway at first follows a valley originating from the first TS and then reaches a VRI point near the second TS where the valley turns into a ridge. With this VRI, we might expect that the reaction path from TS8a$^-$ proceeds to TS8$^-$ without passing through *syn*-8-OO[9MG–H_{N1}]$^-$, *i.e.* reactants → TS8a$^-$ → TS8$^-$ → 4,8-OO-[9MG–H_{N1}]$^-$ + *syn*-8-OO[9MG–H_{N1}]$^-$. This is a scenario that occurred for the ene reaction of $^1O_2$ with alkenes[53] which consists of two adjacent TSs without an intervening intermediate, albeit that the second TS of the ene reaction connects two symmetrically equivalent product minima.

The actual reaction path on the CASSCF surface was identified from the IRC trajectories calculated for TS8a$^-$ and TS8$^-$;

both of which are depicted as dotted lines in Fig. 5e. They clearly show the CASSCF pathway as reactants → TS8a$^-$ → syn-8-OO[9MG–H$_{N1}$]$^-$ → TS8$^-$ → 4,8-OO-[9MG–H$_{N1}$]$^-$. We can now safely conclude that the PES for the formation of 4,8-OO-[9MG–H$_{N1}$]$^-$ favors a two-step mechanism that is preceded by syn-8-OO[9MG–H$_{N1}$]$^-$.

(ii) View of $^1O_2$ addition from direct dynamics. B3LYP/6-31G* was chosen for dynamics simulations of [9MG–H$_{N1}$]$^-$(H$_2$O) + $^1O_2$, since it resulted in reasonable agreement with CASSCF in the overall PES features of [9MG–H$_{N1}$]$^-$ + $^1O_2$. One hundred trajectories were completed at E_{col} = 0.1 eV. All reactive trajectories led to the formation of 8-OO[9MG–H$_{N1}$]$^-$ exclusively. A representative reactive trajectory is illustrated in Fig. 6.

The top frame of Fig. 6 shows the change in potential energy, the approach of reactants as indicated by r(C4–O) and r(C8–O), and the separation of products as by the center-of-mass distance r([9MG–H]$^-$–H$_2$O) between 9MG and water over the trajectory time t = 0–4400 fs. High-frequency oscillations of bond lengths reflect the vibrations of reactants and products. The trajectory forms a syn-8-OO[9MG–H$_{N1}$]$^-$(H$_2$O) at 1.7 ps, followed by elimination of water that occurred at 3.5 ps. By the
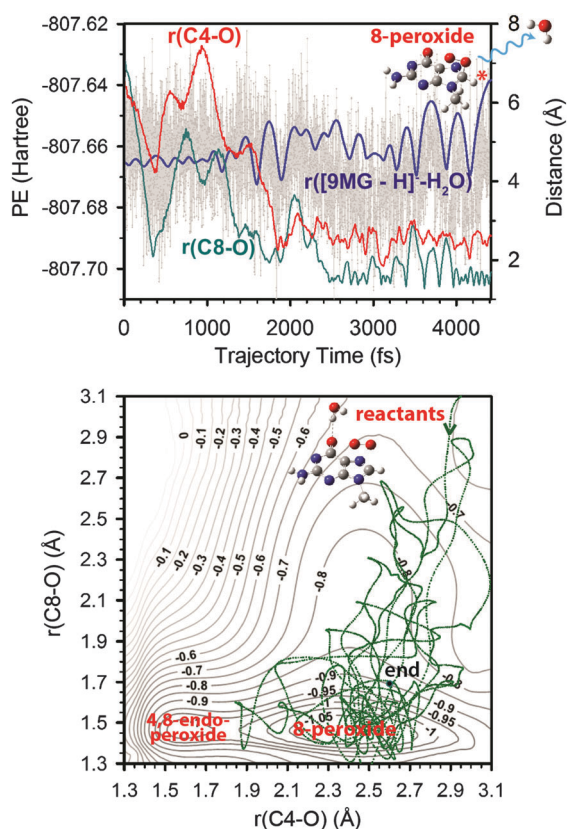
end of the trajectory, the structure of syn-8-OO[9MG–H$_{N1}$]$^-$ remains, and the water is separated from 8-OO[9MG–H$_{N1}$]$^-$ by 6.5 Å. Reaction progress is more clearly illustrated by projecting the trajectory onto the B3LYP/6-31+G* calculated 2D PES (the bottom frame of Fig. 6). As expected, the trajectory does not exactly follow the minimum energy pathway due to accompanying translational and vibrational energy, but overall it descends the PES. No formation of 4,8-OO-[9MG–H$_{N1}$]$^-$ was observed during trajectory time, albeit this cannot be ruled out if the trajectory was propagated over a significantly long period.

Trajectory simulations took into account experimental conditions including E_{col}, temperature, reactant and product vibrations, and the release of energy from ion–molecule reactions, all of which were being excluded in PES analysis. More importantly, direct dynamics calculated the potential energy and energy gradients "on the fly" using quantum chemistry methods;[51,61–63] and the motion of molecules was followed allowing the molecules to show us the preferred pathway. Consequently, trajectory results represent a more realistic picture of the actual experiment.

Note that, compared to CASSCF, B3LYP underestimated the relative energy of 4,8-OO-[9MG–H$_{N1}$]$^-$ by 0.14 eV and thus reversed the stability order of 4,8-OO-[9MG–H$_{N1}$]$^-$ $vs.$ syn-8-OO[9MG–H$_{N1}$]$^-$. This may affect the availability of the phase space in the endoperoxide region. But the influence of this energy shift is minor considering that B3LYP removed the activation barrier leading from syn-8-OO[9MG–H$_{N1}$]$^-$ to 4,8-OO-[9MG–H$_{N1}$]$^-$. The fact that reactive trajectories favor the PES region of hydroperoxide further supported the dynamic importance of hydroperoxide. It follows that the cross section of [9MG–H$_{N1}$]$^-$(H$_2$O) + $^1O_2$ in Fig. 2b was largely determined by the probability of forming 8-OO[9MG–H$_{N1}$]$^-$.

3.3 Implication for oxidation of guanosine *vs.* guanine

We have included in Fig. 2 our recent experimental results of [G + H]$^+$(H$_2$O) and [G–H]$^-$(H$_2$O) + $^1O_2$, whose products were calculated to be 5,8-OO-[G + H]$^+$ and 5,8-OO-[G–H]$^-$ + H$_2$O,[26] respectively. Data are presented in percent reaction efficiency to allow a more effective comparison. Obviously, oxidation of protonated/deprotonated guanine was strongly inhibited (by a factor of 1.5–2) with the 9-methyl substitution.

The comparison of the oxidation pathways of 9MG and guanine in different ionization and hydration states is more informative, from which the resemblances and differences between the oxidation of guanosine and guanine might be extrapolated. In the case of protonated guanine, the 9-methyl substituent does not change the oxidation behavior as far as the $^1O_2$ addition mechanism and the product structure are concerned. The reaction PES for [9MG + H$_{N7}$]$^+$ is in general agreement with that for [G + H]$^+$.[26] The common features include a concerted $^1O_2$ cycloaddition to the imidazole ring giving rise to the formation of a 5,8-endoperoxide, and its subsequent rearrangement to final products 8-oxoG, Gh and Sp or the analogues. Nevertheless, this is not the case for deprotonated systems. Unlike [G–H]$^-$ which follows the same cycloaddition pathway to a similar 5,8-endoperoxide as its

Fig. 6 A representative trajectory of [9MG–H$_{N1}$]$^-$(H$_2$O) + $^1O_2$, showing the formation of an 8-OO[9MG–H$_{N1}$]$^-$(H$_2$O), followed by water elimination. (top) The variation of potential energy, r(C4–O), r(C8–O) and the center-of-mass distance between [9MG–H$_{N1}$]$^-$ and the water ligand during the trajectory. (bottom) Projection of the trajectory (green line) onto the UB3LYP/6-31+G* calculated PES. A video of the trajectory is provided in the ESI.†

15232 | *Phys. Chem. Chem. Phys.*, 2016, **18**, 15223–15234

This journal is © the Owner Societies 2016

protonated counterpart, deprotonated 9MG adopts different steps to initiate $^1O_2$ addition. The reaction proceeds stepwise with the formation of an 8-peroxide as the first step, and the latter evolves to a 4,8-endoperoxide rather than a 5,8-endoperoxide.

Reaction profiles and product structures of deprotonated 9MG are particularly affected by hydration. These can be attributed to the different global minima of deprotonated 9MG in the absence and in the presence of water. Overall, the 9-substitution makes the oxidation of guanine much more dependent on its ionization and hydration states.

4 Conclusions

Guanine is the most easily oxidized of the four DNA bases. Singlet O_2-mediated oxidation of guanine nucleoside is thought to be initiated by the formation of a 4,8-endoperoxide via a [4+2] Diels–Alder cycloaddition—a widely accepted mechanism under neutral conditions as summarized in Scheme 1. In the present study, we used the reaction of 9-methylguanine with $^1O_2$ as a model system to mimic $^1O_2$ oxidation of guanosine in different ionization and hydration states. On the basis of mass spectrometric measurements augmented with molecular potentials and dynamics simulations using both mono-reference (B3LYP, ωB97XD, M06-2X and CCSD(T)//B3LYP) and multi-reference computational methods (CASSCF(10,8) and CASMP2//CASSCF(10,8)), we found that the actual oxidation mechanism and dynamics become more complex when the reactant undergoes oxidation and ionization concurrently. $^1O_2$ oxidation of protonated 9-methylguanine is initiated by the formation of a 5,8-endoperoxide via a concerted cycloaddition, while the initial stage of deprotonated 9-methylguanine switches to an addition of O_2 to the C8 position only. Neither of these follows the reaction pathway of neutral guanosine that is envisioned by Scheme 1. These findings imply that acidic/basic reaction medium must be taken into account in considering the oxidation mechanism and dynamics of guanine nucleoside in aqueous solutions, starting from initial stage.

Acknowledgements

References

1 M. J. Davies, *Biochem. Biophys. Res. Commun.*, 2003, **305**, 761–770.

2 L. J. Marnett and P. C. Burcham, *Chem. Res. Toxicol.*, 1993, **6**, 771–785.

3 C. J. Burrows and J. G. Muller, *Chem. Rev.*, 1998, **98**, 1109–1151.

4 B. Armitage, *Chem. Rev.*, 1998, **98**, 1171–1200.

5 G. Palumbo, *Expert Opin. Drug Delivery*, 2007, **4**, 131–148.

6 J. Cadet, J.-L. Ravanat, G. R. Martinez, M. H. G. Medeiros and P. D. Mascio, *Photochem. Photobiol.*, 2006, **82**, 1219–1225.

7 Y. Ye, J. G. Muller, W. Luo, C. L. Mayne, A. J. Shallop, R. A. Jones and C. J. Burrows, *J. Am. Chem. Soc.*, 2003, **125**, 13926–13927.

8 G. R. Martinez, J.-L. Ravanat, J. Cadet, M. H. Gennari de Medeiros and P. Di Mascio, *J. Mass Spectrom.*, 2007, **42**, 1326–1332.

9 Y. Ye, J. G. Muller and C. J. Burrows, *J. Org. Chem.*, 2006, **71**, 2181–2184.

10 C. Sheu and C. S. Foote, *J. Am. Chem. Soc.*, 1993, **115**, 10446–10447.

11 P. Kang and C. S. Foote, *J. Am. Chem. Soc.*, 2002, **124**, 4865–4873.

12 C. Sheu, P. Kang, S. Khan and C. S. Foote, *J. Am. Chem. Soc.*, 2002, **124**, 3905–3913.

13 R. Grüber, A. Monari and E. Dumont, *J. Phys. Chem. A*, 2014, **118**, 11612–11619.

14 E. Dumont, R. Gruber, E. Bignon, C. Morell, Y. Moreau, A. Monari and J.-L. Ravanat, *Nucleic Acids Res.*, 2016, **44**, 56–62.

15 Y. H. Jang, W. A. Goddard III, K. T. Noyes, L. C. Sowers, S. Hwang and D. S. Chung, *J. Phys. Chem. B*, 2003, **107**, 344–357.

16 Y. Huang and H. Kenttamaa, *J. Phys. Chem. A*, 2004, **108**, 4485–4490.

17 J. D. Zhang, Y. Xie and H. F. Schaefer III, *J. Phys. Chem. A*, 2006, **110**, 12010–12016.

18 E. C. M. Chen, C. Herder and E. S. Chen, *J. Mol. Struct.*, 2006, **798**, 126–133.

19 M. C. Lind, P. P. Bera, N. A. Richardson, S. E. Wheeler and H. F. Schaefer III, *Proc. Natl. Acad. Sci. U. S. A.*, 2006, **103**, 7554–7559.

20 Y. Lin, H. Wang, S. Gao and H. F. Schaefer III, *J. Phys. Chem. B*, 2011, **115**, 11746–11756.

21 G. P. Ford and B. Wang, *Int. J. Quantum Chem.*, 1992, **44**, 587–603.

22 J. Florian and J. Leszczynski, *J. Am. Chem. Soc.*, 1996, **118**, 3010–3017.

23 R. R. Sinden, C. E. Pearson, V. N. Potaman and D. W. Ussery, *Adv. Genome Biol.*, 1998, **5A**, 1–141.

24 I. Rosenthal and J. J. N. Pitts, *Biophys. J.*, 1971, **11**, 963–966.

25 S. Jain, A. Kushwah, P. K. Paliwal and G. N. Babu, *Int. J. Chem. Sci.*, 2010, **8**, 763–768.

26 W. Lu and J. Liu, *Chem. – Eur. J.*, 2016, **22**, 3127–3138.

27 M. Freccero, R. Gandolfi and M. Sarzi-Amade, *J. Org. Chem.*, 2003, **68**, 6411–6423.

28 W. Chin, M. Mons, F. Piuzzi, B. Tardivel, I. Dimicoli, L. Gorb and J. Leszczynski, *J. Phys. Chem. A*, 2004, **108**, 8237–8243.

29 B. H. Munk, C. J. Burrows and H. B. Schlegel, *Chem. Res. Toxicol.*, 2007, **20**, 432–444.

30 H. Saigusa, S.-h. Urashima and H. Asami, *J. Phys. Chem. A*, 2009, **113**, 3455–3462.

31 L. Feketeová, G. N. Khairallah, B. Chan, V. Steinmetz, P. Maître, L. Radom and R. A. J. O'Hair, *Chem. Commun.*, 2013, **49**, 7343–7345.

32 J. Gonzalez, I. Banos, I. Leon, J. Contreras-Garcia, E. J. Cocinero, A. Lesarri, J. A. Fernandez and J. Millan, *J. Chem. Theory Comput.*, 2016, **12**, 523–534.

33 B. Song, J. Zhao, R. Griesser, C. Meiser, H. Sigel and B. Lippert, *Chem. – Eur. J.*, 1999, **5**, 2374–2387.

34 G. M. Blackburn, M. J. Gait, D. Loakes and D. M. Williams, *Nucleic Acids in Chemistry and Biology*, Royal Society of Chemistry, Cambridge, UK, 2006.

35 A. Domínguez-Martín, S. Johannsen, A. Sigel, B. P. Operschall, B. Song, H. Sigel, A. Okruszek, J. M. González-Pérez, J. Niclós-Gutiérrez and R. K. O. Sigel, *Chem. – Eur. J.*, 2013, **19**, 8163–8181.

36 I. Velikyan, S. Acharya, A. Trifonova, A. Foeldesi and J. Chattopadhyaya, *J. Am. Chem. Soc.*, 2001, **123**, 2893–2894.

37 Y. Fang and J. Liu, *J. Phys. Chem. A*, 2009, **113**, 11250–11261.

38 C. S. Foote, *Science*, 1968, **162**, 963–970.

39 A. Midey, I. Dotan and A. A. Viggiano, *J. Phys. Chem. A*, 2008, **112**, 3040–3045.

40 Y. Fang, F. Liu, A. Bennett, S. Ara and J. Liu, *J. Phys. Chem. B*, 2011, **115**, 2671–2682.

41 W. J. Lafferty, A. M. Solodov, C. L. Lugez and G. T. Fraser, *Appl. Opt.*, 1998, **37**, 2264–2270.

42 F. Liu, Y. Fang, Y. Chen and J. Liu, *J. Phys. Chem. B*, 2012, **116**, 6369–6379.

43 M. J. Frisch, G. W. Trucks, H. B. Schlegel, G. E. Scuseria, M. A. Robb, J. R. Cheeseman, G. Scalmani, V. Barone, B. Mennucci, G. A. Petersson, H. Nakatsuji, M. Caricato, X. Li, H. P. Hratchian, A. F. Izmaylov, J. Bloino, G. Zheng, J. L. Sonnenberg, M. Hada, M. Ehara, K. Toyota, R. Fukuda, J. Hasegawa, M. Ishida, T. Nakajima, Y. Honda, O. Kitao, H. Nakai, T. Vreven, J. J. A. Montgomery, J. E. Peralta, F. Ogliaro, M. Bearpark, J. J. Heyd, E. Brothers, K. N. Kudin, V. N. Staroverov, T. Keith, R. Kobayashi, J. Normand, K. Raghavachari, A. Rendell, J. C. Burant, S. S. Iyengar, J. Tomasi, M. Cossi, N. Rega, J. M. Millam, M. Klene, J. E. Knox, J. B. Cross, V. Bakken, C. Adamo, J. Jaramillo, R. Gomperts, R. E. Stratmann, O. Yazyev, A. J. Austin, R. Cammi, C. Pomelli, J. W. Ochterski, R. L. Martin, K. Morokuma, V. G. Zakrzewski, G. A. Voth, P. Salvador, J. J. Dannenberg, S. Dapprich, A. D. Daniels, O. Farkas, J. B. Foresman, J. V. Ortiz, J. Cioslowski and D. J. Fox, *Gaussian 09, Revision D.01*, Gaussian, Inc., Wallingford, CT, 2013.

44 X. Zou, H. Zhao, Y. Yu and H. Su, *J. Am. Chem. Soc.*, 2013, **135**, 4509–4515.

45 J. Méndez-Hurtado, R. López, D. Suárez and M. I. Menéndez, *Eur. J. Chem.*, 2012, **18**, 8437–8447.

46 T. J. Lee and P. R. Taylor, *Int. J. Quantum Chem., Quantum Chem. Symp.*, 1989, **23**, 199–207.

47 R. A. Marcus, *J. Chem. Phys.*, 1952, **20**, 359–364.

48 I. M. Alecu, J. Zheng, Y. Zhao and D. G. Truhlar, *J. Chem. Theory Comput.*, 2010, **6**, 2872–2887.

49 L. Zhu and W. L. Hase, *A General RRKM Program(QCPE 644), Quantum Chemistry Program Exchange*, Chemistry Department, University of Indiana, Bloomington, 1993.

50 W. L. Hase, K. Bolton, P. de Sainte Claire, R. J. Duchovic, X. Hu, A. Komornicki, G. Li, K. Lim, D. Lu, G. H. Peslherbe, K. Song, K. N. Swamy, S. R. Vande Linde, A. Varandas, H. Wang and R. J. Wolf, *VENUS 99: a general chemical dynamics computer program*, Texas Tech Univeristy Lubbock, TX, 1999.

51 V. Bakken, J. M. Millam and H. B. Schlegel, *J. Chem. Phys.*, 1999, **111**, 8773–8777.

52 B. Thapa and H. B. Schlegel, *J. Phys. Chem. A*, 2015, **119**, 5134–5144.

53 D. A. Singleton, C. Hang, M. J. Szymanski, M. P. Meyer, A. G. Leach, K. T. Kuwata, J. S. Chen, A. Greer, C. S. Foote and K. N. Houk, *J. Am. Chem. Soc.*, 2003, **125**, 1319–1328.

54 M. Bobrowski, A. Liwo, S. Oldziej, D. Jeziorek and T. Ossowski, *J. Am. Chem. Soc.*, 2000, **122**, 8112–8119.

55 B. H. Munk, C. J. Burrows and H. B. Schlegel, *J. Am. Chem. Soc.*, 2008, **130**, 5245–5256.

56 F. Liu, W. Lu, Y. Fang and J. Liu, *Phys. Chem. Chem. Phys.*, 2014, **16**, 22179–22191.

57 J. Troe, *Chem. Phys. Lett.*, 1985, **122**, 425–430.

58 P. B. Armentrout, *J. Anal. At. Spectrom.*, 2004, **19**, 571–580.

59 P. Valtazanos, S. T. Elbert and K. Ruedenberg, *J. Am. Chem. Soc.*, 1986, **108**, 3147–3149.

60 P. Valtazanos and K. Ruedenberg, *Theor. Chim. Acta*, 1986, **69**, 281–307.

61 K. K. Baldridge, M. S. Gordon, R. Steckler and D. G. Truhlar, *J. Phys. Chem.*, 1989, **93**, 5107–5119.

62 T. Helgaker, E. Uggerud and H. J. A. Jensen, *Chem. Phys. Lett.*, 1990, **173**, 145–150.

63 *Advances in Classical Trajectory Methods, Vol. 1: Intramolecular and Nonlinear Dynamics*, ed. W. L. Hase, JAI, Greenwich, 1998.

15234 | *Phys. Chem. Chem. Phys.*, 2016, **18**, 15223–15234

This journal is © the Owner Societies 2016